Terahertz Semiconductor Quantum Well Devices *

Liu H C[1,†], Luo H[1], Ban D[1], Wächter M[1], Song C Y[1], Wasilewski Z R[1], Buchanan M[1], Aers G C[1], SpringThorpe A J[1], Cao J C[2], Feng S L[2], Williams B S[3], and Hu Q[3]

(1 *Institute for Microstructural Sciences, National Research Council, Ottawa K1A 0R6, Canada*)
(2 *State Key Laboratory of Functional Materials for Informatics, Shanghai Institute of Microsystem and Information Technology, Chinese Academy of Sciences, Shanghai 200050, China*)
(3 *Department of Electrical Engineering and Computer Science and Research Laboratory of Electronics, Massachusetts Institute of Technology, Cambridge, Massachusetts 02139, USA*)

Abstract: For eventually providing terahertz science with compact and convenient devices, terahertz (1～10THz) quantum-well photodetectors and quantum-cascade lasers are investigated. The design and projected detector performance are presented together with experimental results for several test devices, all working at photon energies below and around optical phonons. Background limited infrared performance (BLIP) operations are observed for all samples (three in total), designed for different wavelengths. BLIP temperatures of 17, 13, and 12K are achieved for peak detection frequencies of 9.7THz (31μm), 5.4THz (56μm), and 3.2THz (93μm), respectively. A set of THz quantum-cascade lasers with identical device parameters except for doping concentration is studied. The δ-doping density for each period varies from 3.2×10^{10} to $4.8\times10^{10}\,cm^{-2}$. We observe that the lasing threshold current density increases monotonically with doping concentration. Moreover, the measurements for devices with different cavity lengths provide evidence that the free carrier absorption causes the waveguide loss also to increase monotonically. Interestingly the observed maximum lasing temperature is best at a doping density of $3.6\times10^{10}\,cm^{-2}$.

Key words: terahertz; quantum well photodetector; quantum-cascade laser
EEACC: 7230C; 4320J
CLC number: TN2 **Document code:** A **Article ID:** 0253-4177(2006)04-0627-08

1 Introduction

Terahertz (THz) science and technology have attracted much recent attention[1,2]. The THz region is loosely defined as the range of frequencies from 1 to 10THz (wavelengths from 30 to 300μm or energies from 4.1 to 41meV). THz frequencies fall partly into the far-infrared spectrum and partly into the submillimeter wave band. Although many proof-of-concept experiments have been carried out, demonstrating potential applications of THz technology[1～3], the lack of compact and convenient THz generation and detection devices needs to be addressed before widespread applications become a reality. This paper reports our recent efforts in the research and development of both THz quantum-well photodetectors and quantum-cascade lasers (QCL).

2 THz quantum-well photodetectors

2.1 Design considerations

For the infrared spectrum, quantum-well infrared photodetectors[4] (QWIPs) are well established. Here we extend the wavelength coverage of QWIPs into the THz region. QWIP materials are commonly GaAs/AlGaAs[4]. The high absorption by optical phonons of GaAs makes the region of 34～36meV (34～36μm or 8～9THz) inaccessible. Quantum-well designs using GaAs/AlGaAs are well known for mid-infrared QWIPs[4]. In the THz region, if we apply the same principle of having the first excited state in resonance with the top of the barrier, the calculated optimum quantum-well parameters are shown in Fig. 1. The calculation is a simple one, using the one-parabolic-band effective-

* Project supported by the NRC GHI Program, the National Fund for Distinguished Young Scholars of China (Nos. 60425415 and 60528005), the Major Project of the National Natural Science Foundation of China (No. 10390162), AFOSR, NASA, and NSF
† Corresponding author. Email: h.c.liu@nrc.ca
Received 13 December 2005

mass approximation. Many-body effects are not included because of the low doping densities used in THz QWIPs. From Fig. 1, we predict that the THz frequency range of 1～8 THz can be covered by QWIPs with low aluminum fractions from 0.8% to 5.4%.

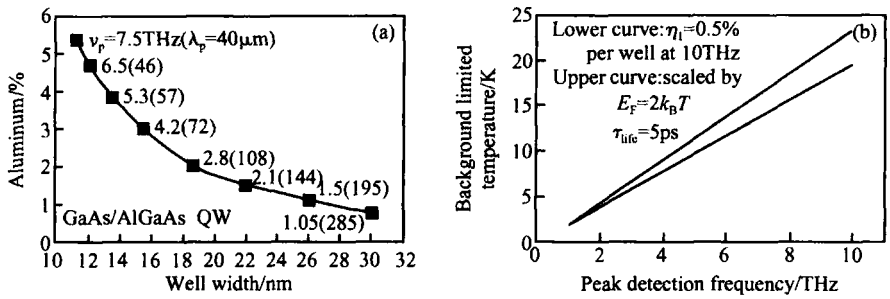

Fig. 1 Quantum well parameters and projected device performance (a) Calculated well width (L_w) and barrier aluminum alloy fraction (x) for an optimized GaAs/AlGaAs quantum well The conduction band offset (barrier height V_b) relates to x by $V_b = 0.87x$(eV). The range covers the peak detection frequency ν_p (or wavelength λ_p) from 1.05(285) to 7.5THz (40μm); (b) Calculated temperature for background limited infrared performance versus peak detection frequency The background temperature is 300K and the field-of-view (FOV) full cone angle is 90°. The upper curve has a lower absorption (by about 10 times) than the lower curve.

In general, a good detector must have sufficiently high absorption. For the intersubband transition in quantum wells, the absorption efficiency is well characterized and easily calculated[4]. High doping is desirable for achieving high absorption, but it leads to a high dark current and low operating temperature. A trade-off[4] must be made for a given application. For most applications, it is desirable to operate the detector under the background-limited condition. The temperature for achieving the background limited infrared performance (T_{blip}) is therefore important. Figure 1 also shows the calculated T_{blip} versus the peak detection frequency. The BLIP temperature is found by equating the calculated dark current and photocurrent caused by the background. The dark current is estimated by multiplying the mobile electron density and drift velocity (the "3D drift model" in Ref. [4]). The device parameters needed in this calculation are excited electron lifetime τ_{life} (taken as 5ps), quantum-well period L_p (taken as 30nm), and absorption efficiency per well η. To achieve the highest dark-current-limited detectivity[4], the two-dimensional electron density n_{2D} should correspond to $E_F = 2k_BT$, where the Fermi energy is given by $E_F = (\pi\hbar^2/m) \times n_{2D}$, m is the effective mass, and T is the operating temperature. For GaAs, $n_{2D} = 5 \times 10^{11}$ cm^{-2} corresponds to about 77K and a one-well polarized absorption of about 0.5%[4]. If one follows the $E_F = 2k_BT$ rule, the density becomes very low for low temperatures (≪77K), making the absorption low as well. We therefore consider two cases in the lower part of Fig. 1. The upper curve uses the $E_F = 2k_BT$ condition, while the lower curve starts with a higher absorption (using higher doping) $\eta = 0.5\%$ at 10THz, and decreases linearly to 0.05% at 1THz. The trade-off here is that if the operating temperature is desired to be as high as possible, the upper curve should be followed. On the other hand, if high absorption is needed, one should follow the lower curve but require slightly more cooling. Reaching the BLIP condition is necessary for detecting weak signals. In some applications involving a strong source such as a THz QCL, the requirement is different. Here as long as the dark current is lower than the signal photocurrent, photon noise limited detection is achieved. In such a case, the detector operating temperature can be raised.

So far, the above analysis assumes that the tunneling contribution (such as direct inter-well, scattering assisted, and hopping-like via deep-impurity levels in the barriers) is negligible. While some of the mechanisms are highly sample-dependent, such as those related to impurity and defect, the magnitude of direct inter-well tunneling is easy to estimate. Figure 2 shows the estimated tunneling current versus barrier thickness for three values of

aluminum fraction x. The expression used for the estimate is $(ev n_{2D}/L_w)D$, where $v = (2E_0/m)^{1/2}$, E_0 is the ground state energy, L_w is the well width, and D is the transmission coefficient calculated using the WKB approximation.

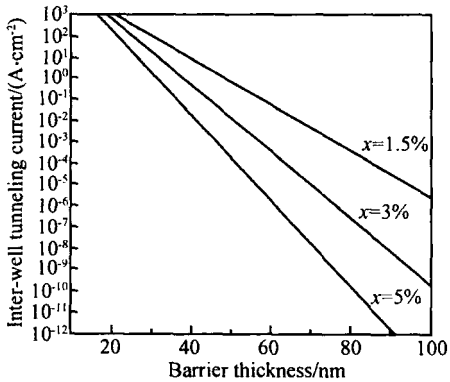

Fig. 2　Estimated direct inter-well tunneling current versus barrier thickness for three cases of barrier aluminum fractions of x = 1.5%, 3%, and 5%　Other parameters used for the estimate are E_0 = 4.3, 8.6, and 14meV, n_{2D} = 0.3 ×10¹¹, 0.6 ×10¹¹, and 1.0 ×10¹¹ cm⁻², and L_w = 22.0, 15.4, and 12.0nm, for the three x values, respectively.

2.2　Experiment and discussion

Under the guidance of the above design considerations, three test samples were fabricated. The sample parameters are listed in Table 1. The wafers were grown by molecular beam epitaxy (MBE) on semi-insulating GaAs substrates. The standard QWIP device consists of a number of GaAs/AlGaAs quantum wells sandwiched between top and bottom contacts. The barrier thickness was designed so the inter-well tunneling currents are below a certain level (~10^{-5} A/cm²), estimated from Fig. 2. The current level of ~10^{-5} A/cm² corresponds to the estimated background current. The center 10nm of each well was doped with Si. The doping values were chosen to be close to the condition for optimizing detectivity. These values give rise to an estimated absorption in the range of a fraction of a percent per well. The top 400nm and bottom 800nm GaAs contact layers were doped with Si to 10^{17} cm⁻³. The relatively low contact doping value was necessary to reduce the contact layer free carrier absorption and plasma reflection in the THz region. The numbers of wells were varied among the three samples to keep the epilayer thickness around 3.5μm.

Table 1　Structure parameters for the THz QWIPs

Sample	L_w/nm	L_b/nm	[Al]	N_d/cm⁻³	N	ν/THz
v265	11.9	55.2	5%	1 ×10¹⁷	40	7.0
v266	15.5	70.2	3%	6 ×10¹⁶	30	4.2
v267	22.1	95.1	1.5%	3 ×10¹⁶	23	2.2

L_w is the well width, L_b is the barrier width, [Al] is the barrier aluminum fraction, N_d is the doping value in the center 10nm of each quantum well, N is the number of quantum wells, and ν is the frequency corresponding to the calculated intersubband transition energy. The GaAs/AlGaAs MQWs are sandwiched between 400nm top and 800nm bottom GaAs contact layers doped with Si to 10^{17} cm⁻³.

Mesa devices of different sizes were fabricated using standard GaAs processing techniques. Test devices were angle-polished to yield a 45° facet and were packaged in the standard double pass backside illumination geometry with a 45° internal incidence angle. The photocurrent spectra at 8K for the three samples are shown in Fig. 3. The polarization rule for intersubband transition was checked with p- and s-polarized light. Photocurrent was observed only under p-polarization, confirming that its origin is from intersubband transition. The response peaks were measured at 322cm⁻¹ (31μm, 9.7THz), 180cm⁻¹ (56μm, 5.4THz), and 108cm⁻¹ (93μm, 3.2THz) for samples v265, v266, and v267, respectively. These agree reasonably well with the design value, considering the uncertainty in the growth and the untested range of very low aluminum fractions for QWIP design. The main dark region from 265 to 297cm⁻¹ (33 to 37meV) is due to GaAs optical phonon absorption. Other smaller features are also correlated to AlGaAs phonon and GaAs multi-phonon absorption processes. Due to the strong phonon absorption, the as-observed peak at 322cm⁻¹ for sample v265 has a large uncertainty. The photoresponse spectra for all three samples are quite broad, indicating that the intersubband transitions are of bound-to-continuum origin. The doping value in the GaAs contact layer (10^{17} cm⁻³) gives rise to a plasma edge frequency of 101cm⁻¹, which may contribute to the relatively sharp decline at the longer wavelength side of about 100cm⁻¹ for sample v267. For all three samples, the spectral shapes are nearly independent of bias voltage up to a certain voltage value. Beyond the voltage limits, the dark currents increase rapidly and the photocurrent spectra become unreliable. The voltage limits are ±0.8, ±0.2, and ±0.03V for samples v265, v266, and v267, respectively.

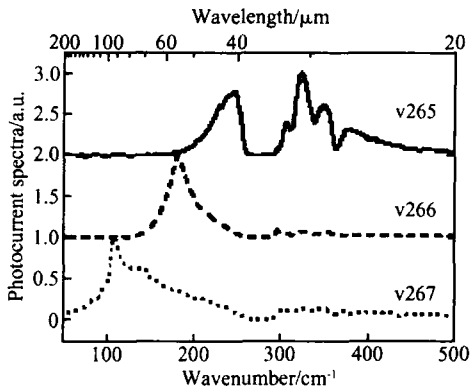

Fig. 3 Normalized photocurrent spectra at 8K The solid curve is for sample v265 at 0. 8V with a peak response at 322cm^{-1} (31μm, 9. 7THz). The dashed curve corresponds to sample v266 at 0. 15V with a peak response at 180cm^{-1} (56μm, 5. 4THz). The dotted curve corresponds to sample v267 at 0. 03V with a peak response at 108cm^{-1} (93μm, 3. 2THz).

The calibrated peak responsivity versus bias voltage at different temperatures is shown in Fig. 4. All three responsivity curves show very similar trends. The responsivity increases nearly linearly with bias from the origin, another indication that the transition is of bound-to-continuum origin. The responsivity-voltage curves are almost independent of temperature up to a certain value. Above this temperature, the responsivity curves show a marked increase. This upward trend may be related to the increase in mobility with temperature in the impurity scattering limited regime. The responsivity values at low temperatures are in the range of 0. 4 to 1. 0A/W, comparable to those from mid-infrared and far-infrared QWIPs[4]. This result implies that the photoconductive gain is similar to those of mid- and far-infrared QWIPs and that the excited carrier lifetimes are also similar.

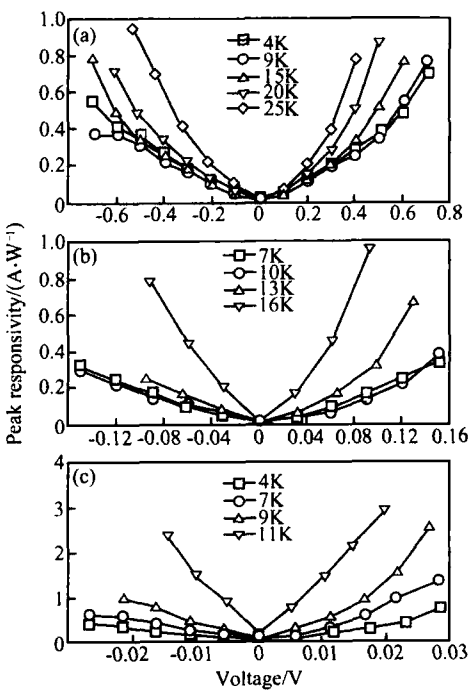

Fig. 4 Peak responsivity versus bias voltage at different temperatures for the three THz QWIP samples (a) Sample v265 at 31μm; (b) Sample v266 at 56μm; (c) Sample v267 at 93μm

BLIP temperatures were measured by comparing current-voltage curves under a dark condition and under a 300K background with a 90° field of view (FOV) at different temperatures. The measured current-voltage curves are shown in Fig. 5. T_{blip} is taken as the temperature at which the background photocurrent equals the dark current. The measured BLIP temperatures are 17, 13, and 12K for samples v265, v266, and v267, respectively. The results agree reasonably well with the calculated values for v265 and v266 in Fig. 1. For sample v267, the measure value of 12K is much higher than the calculated 5K. The reason for this is not known presently. It is interesting to compare the dark current of sample v265 with the previous device[4], which had a similar quantum well structure but a narrower barrier width (40nm). Sample v265 has a much lower current, about three orders lower at temperatures below 17K. We attribute the substantial decrease in dark current to the reduction of inter-well tunneling by employing wider barriers. When the temperature dropped below a certain point, the dark current stopped decreasing and remained the same. This temperature is 14 and 9K for samples v265 and v266, respectively. This bottom-out behavior is due to the remaining inter-well tunneling or other mechanisms. Since these tunneling currents are much lower than the background photocurrent, they do not affect device performance under normal background limited operation. For sample v267, because thermionic emission and field assisted tunneling were much stronger than inter-well tunneling within the experiment temperature range, we did not observe any current bottom-out behavior.

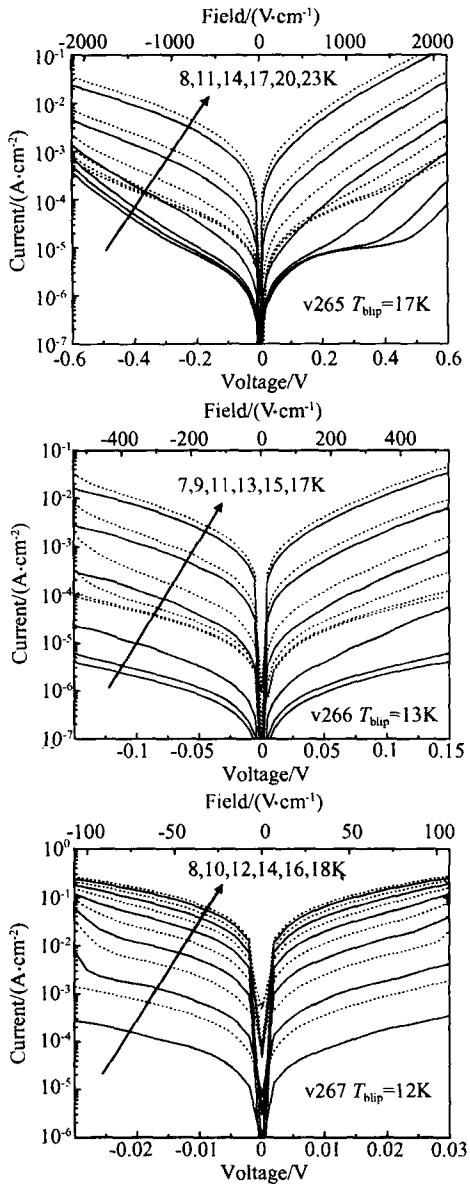

Fig. 5 Current voltage curves under dark condition (solid) and under a 90° FOV 300 K background (dash)

2.3 Conclusion of this section

To end this section, working towards a high-performance THz QWIP technology, we have discussed the design parameters and projected characteristics and presented the experimental results for a set of test devices. We have demonstrated BLIP operations of three QWIPs with different detection wavelengths in the terahertz region. Increasing barrier thickness is found to be an effective method for reducing the dark current and enabling BLIP operation. BLIP temperatures of 17, 13, and 12 K were achieved for peak detection wavelengths of 31, 56, and 94 μm, respectively.

3 THz quantum-cascade lasers

3.1 Device design

During the past three years, the most exciting new development in semiconductor physics and devices is the THz QCL. It has seen very significant progress since the first report in 2002[6~12]. Along with the rapid advances, a good qualitative physical picture of the device operation is emerging, including critical processes such as carrier relaxation, tunneling, and dephasing. Based on our current understanding, while we are able to choose the values of most device parameters, we are not able to predict the optimal doping for a given design. In this section, we present a systematic study of the effect of doping on the performance of THz QCLs.

At present, there are two basic designs of THz QCLs, but there are surely more to come, either with[8,9,11] or without[6,7,10,12] the explicit phonon resonant relaxation. The active region of the QCL wafer, similar to Ref. [11], is based on a 4-well module design in which the THz generating transition is from a pair of anti-crossed double-well states, the longitudinal-optical (LO) phonon mediated relaxation occurs in a wide and doped subsequent well, and the injection to the following double well is from an undoped well. A schematic of the conduction band profile is shown on the left part of Fig. 6, together with the calculated squared wavefunctions of the most relevant states. In order to isolate the effects solely due to doping, it is crucial to keep all other parameters, including Al fraction and layer (well and barrier) thicknesses, unchanged while varying the doping concentration. A special MBE growth procedure was employed. We used δ-doping with Si at the center of the 15nm-thick "phonon" well and stopped the wafer rotation only during the doping, each time precisely aligning the wafer's [011] crystallographic direction along the Si cell azimuthal orientation (see Fig. 6). This resulted in a nearly linear gradient of the doping concentration across the 75mm wafer, which had identical layer thicknesses and aluminum fraction. The QCL wafer was grown on a semi-insulating GaAs substrate with 176-cascaded 4-well modules made of GaAs wells and $Al_{0.15}Ga_{0.85}As$ barriers.

Cladding and contact layers were the same as those in Ref. [11], except that the etch-stop layer was 0.1μm-thick AlAs and the lower contact layer was 0.1μm-thick n^+ GaAs, doped with Si to 5.0×10^{18} cm^{-3}. Beginning with the first injection barrier, the layer thicknesses of the 4-well module are **5.4**/7.8/**2.4**/6.4/**3.8**/<u>15.3</u>/**3.5**/8.8nm, where the barrier layers are shown in bold and the doped layer is underlined. A schematic of the wafer and the positions of the measured samples are shown on the right part of Fig. 6.

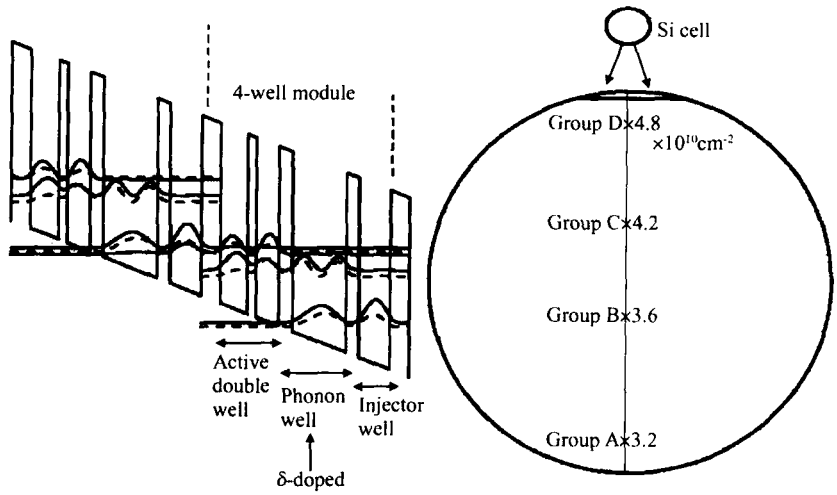

Fig. 6 Schematic conduction band profile, calculated wavefunctions, and schematic wafer layout

3.2 Experiment and discussion

Four small pieces (labeled A～D) were used systematically for this study. By secondary ion mass spectroscopy (SIMS) measurements, their δ-doping densities were determined to be 3.2×10^{10} cm^{-2} (Sample A), 3.6×10^{10} cm^{-2} (B), 4.2×10^{10} cm^{-2} (C), and 4.8×10^{10} cm^{-2} (D), respectively. The nearly linear variation across the wafer is in good agreement with theoretical modeling[13]. The doping density and key measured results are listed in Table 2. The samples (A to D) were fabricated in high-confinement metal-metal waveguides using In-Au metallic wafer bonding as described in Ref. [11]. Lasers with various ridge widths (ranging from 40 to 200μm) and cavity lengths (1～2mm) were tested. No coatings were applied on the cleaved facets. All lasers were biased in pulsed mode with a pulse width of 1μs and repetition rate of 1kHz.

Table 2 Doping parameters and measured results for a set of four samples

Sample	A	B	C	D
δ-doping density / $10^{10}cm^{-2}$	3.2	3.6	4.2	4.8
Threshold current density / ($A\cdot cm^{-2}$)	255	408	580	800
Maximum lasing temperature/ K	90	109	88	79

The last two rows list the threshold current density at 10K and in the infinite cavity length limit, and the maximum lasing temperature taken as the mean value of all measured data from each group.

Measurements of electrical and optical characteristics of the fabricated QCLs were carried out at cryogenic heat-sink temperatures (10 to 120K). Figure 7(a) shows the temperature-dependent light versus current density curves of one device cut from sample C. The threshold current density J_{th} of this device is around $720A/cm^2$ at 10K and increases with temperature. The inset in Fig. 7 shows a typical lasing spectrum measured at 10K, which peaks at a wavelength of 103.6μm, corresponding to 2.9THz in frequency. Figure 7(b) shows the measured current versus voltage characteristics at various temperatures.

For different groups of devices, Figure 8 shows the threshold current density versus the heat-sink temperature. Different curves within each group result from devices with different cavity lengths and ridge widths, respectively. The spread represents the uncertainty of this experiment. It is clear that devices with the lowest δ-doping concen-

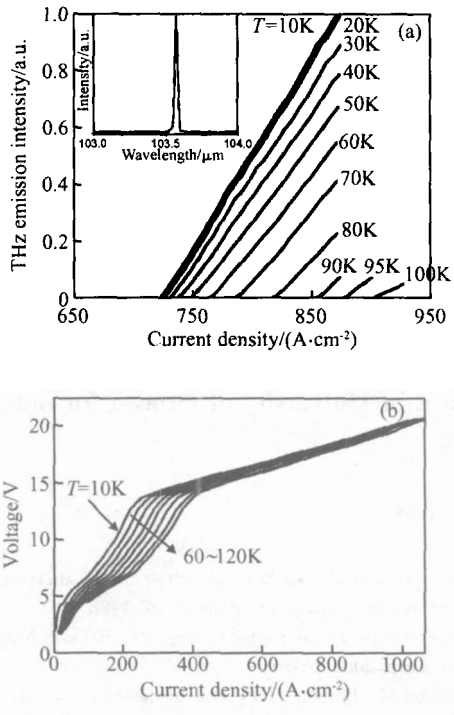

Fig. 7 Lasing light-current (a) and voltage-current (b) curves at different temperatures for a typical QCL device The inset shows a lasing spectrum. The device was biased at 632A/cm^2 in pulsed mode (pulse width 1μs and repetition rate 1kHz) at 10K.

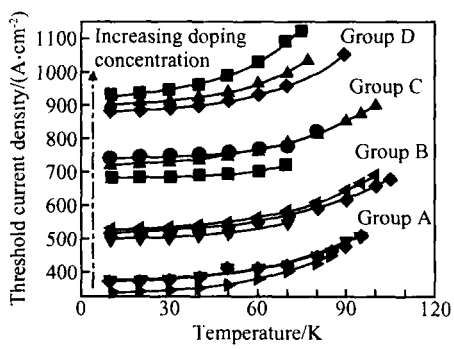

Fig. 8 Threshold current density as a function of heat-sink temperature for the four groups of devices with different device dimensions (cavity length and ridge width)

tration (Sample A) have the lowest threshold current density, while J_{th} is highest for those with the highest δ-doping concentration (Sample D). Figure 9 plots the threshold current density at 10K for devices with different cavity lengths as a function of the reciprocal cavity length $1/L$. The thresholds in the limit of infinite cavity length ($1/L \to 0$) are given in Table 2. As expected, the threshold current density increases with $1/L$ for all four groups. The

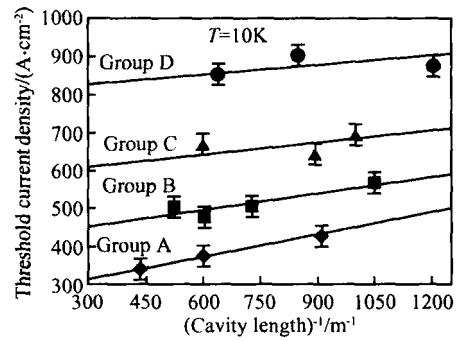

Fig. 9 Threshold current density at 10K as a function of reciprocal cavity length The symbols show experimental data and the solid lines are linear fits.

behavior displayed in Figs. 8 and 9 is consistent with a monotonic increase of the waveguide loss as the doping concentration is increased. Unfortunately, we cannot extract the waveguide loss reliably, as it would require the accurate determination of the transparency current density and the parasitic current as well as the mirror loss. For the present metal-metal waveguide, similar to the microstrip transmission line——a common microwave technique, the mirror loss is more complicated to simulate than the usual dielectric waveguide. Recent electro-magnetic simulations by Kohen *et al*. predicted a reflectivity value in the range of 0.76 ~ 0.85[14], which is very different from that of about 0.3 calculated by an effective index of about 3.5.

Thus far the general trends of the measured results are not surprising: Increasing doping results in an increase in free carrier absorption and waveguide loss and therefore an increase in the threshold current density. It is clear that the two extremes of no doping and extremely high doping are of no practical use. There must be an optimum region of doping for certain device characteristics. One of the most important figures-of-merit is the maximum operating temperature T_{max}, which depends on the range of current densities for which lasing occurs, i.e. $J_{max} - J_{th}$, where J_{max} is the maximum current density for which lasing occurs. Beyond this J_{max}, subband misalignment happens and lasing ceases. Increasing the doping concentration increases both J_{th} and J_{max}, but there is an optimum doping which yields the highest T_{max}. Figure 10 shows the observed maximum lasing temperature T_{max} of the four groups of QCLs as a function of δ-doping density. It clearly shows the existence of an

optimum δ-doping density (~3.6 ×10^{10} cm^{-2}) for achieving the highest maximum lasing temperature. Note that each of the experimental points in Fig. 10 is the average of results from several devices, and the error bars are the results of statistical analysis. In addition to T_{max}, we also analyzed T_0 for all devices, but no trend was found.

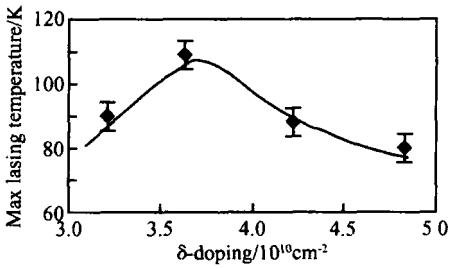

Fig. 10 Measured maximum lasing temperature as a function of δ-doping concentration. The maximum temperature was measured in pulsed mode by increasing heat-sink temperature until the lasing operation could not be observed. The symbols are measured results and the line is a guide to the eye.

Although the observed results are not unexpected, we do not have a quantitative theoretical explanation. We hope that future advances in modeling will provide the interpretation and the prediction capability necessary for the design of THz QCLs. Clearly, more investigations are in order.

3.3 Conclusion of this section

In summary of this section, a series of THz QCLs with different δ-doping concentrations in the active region have been fabricated and characterized. Experimental results show that the lasing threshold current density depends strongly on the doping concentration. The results also indicate that the waveguide loss increases with doping. The maximum lasing temperature displays an optimum for a doping density of 3.6 ×10^{10} cm^{-2}. Our results point out the critical role that the doping concentration plays in reaching high temperature operation.

4 Couclusion

As an end note of this paper, although substantial follow-up work is needed, we are optimistic that we will further improve the device performance, and we project that optimized THz quantum devices will be useful for the booming field of THz science and technology and create new and unique applications.

Acknowledgments The authors thank Aslan B, Dupont E, and Grant P D for helpful discussions, Barrios P, Bezinger A, Dudek R, Froemel J, Malloy M, Marshall P, and Wang R for technical assistance, Sproule G I for SIMS measurements, and Fortin E of University of Ottawa for indium deposition.

References

[1] Ferguson B, Zhang X C. Materials for terahertz science and technology. Nature Materials, 2002, 1: 26
[2] Siegel P H. Terahertz technology. IEEE Trans Microw Theory Tech, 2002, 50: 910
[3] Nagel M, Bolivar H P, Brucherseifer M, et al. Integrated THz technology for label-free genetic diagnostics. Appl Phys Lett, 2002, 80: 154
[4] Liu H C. Quantum well infrared photodetector physics and novel devices. In: Liu H C, Capasso F, ed. Semiconductors and semimetals, Vol. 62: Intersubband transition in quantum wells: physics and device applications I. San Diego: Academic Press, 2000: 126
[5] Liu H C, Song C Y, SpringThorpe A J, et al. Terahertz quantum-well photodetector. Appl Phys Lett, 2004, 84: 4068
[6] Köhler R, Treicucci A, Beltram F, et al. Terahertz semiconductor-heterostructure laser. Nature, 2002, 417: 156
[7] Rochat M, Ajili L, Willenberg H, et al. Low-threshold terahertz quantum-cascade lasers. Appl Phys Lett, 2002, 81: 1381
[8] Williams B S, Callebaut H, Kumar S, et al. Terahertz quantum-cascade laser at λ~100mm using metal waveguide for mode confinement. Appl Phys Lett, 2003, 83: 2124
[9] Williams B S, Kumar S, Callebaut H, et al. Terahertz quantum-cascade laser operating up to 137K. Appl Phys Lett, 2003, 83: 5142
[10] Köhler R, Tredicucci A, Beltram F, et al. High-performance continuous-wave operation of superlattice terahertz quantum-cascade lasers. Appl Phys Lett, 2003, 82: 1518
[11] Kumar S, Williams B S, Kohen S, et al. Continuous-wave operation of terahertz quantum-cascade lasers above liquid-nitrogen temperature. Appl Phys Lett, 2004, 84: 2494
[12] Barbieri S, Alton J, Beere H E, et al. 2.9THz quantum cascade lasers operating up to 70K in continuous wave. Appl Phys Lett, 2004, 85: 1674
[13] Wasilewski Z R, Aers G C, SpringThorpe A J, et al. Studies and modeling of growth uniformity in molecular beam epitaxy. J Vac Sci Technol B, 1991, 9: 120
[14] Kohen S, Williams B S, Hu Q. Electromagnetic modeling of terahertz quantum cascade laser waveguides and resonators. J Appl Phys, 2005, 97: 053106